DOI 10.1007/s11106-023-00367-4
Powder Metallurgy and Metal Ceramics, Vol. 62, Nos. 1-2, May, 2023 (Russian Original Vol. 62, Nos. 1-2, Jan.-Feb., 2023)

THEORY AND TECHNOLOGY OF SINTERING, THERMAL AND THERMOCHEMICAL TREATMENT

DENSIFICATION KINETICS OF THE TiB_2–20 wt.% $MoSi_2$ COMPOSITE DURING NONISOTHERMAL SPARK PLASMA SINTERING

M.S. Kovalchenko,[1,2] R.V. Lytvyn,[1] I.V. Kud,[1] and O.B. Zgalat-Lozynskyy[1]

UDC 621.365.32:621.762.02/.05:546.[271'82+281'77]

The densification of a powder mixture containing titanium diboride and 20 wt.% molybdenum disilicide during nonisothermal spark plasma sintering was experimentally studied. The sintering process was assisted with an external pressure of 50.93 MPa in vacuum at a controlled constant heating rate of 1.67 and 2.72 K per second. It was established that sintering occurred when the thermodynamic temperature reached 1155 K, which should be taken as the critical brittle–ductile transition temperature for molybdenum disilicide, a less refractory material. The densification kinetics was analyzed using the continuum theory for bulk viscous flow of a porous body, considering the effect of powder particle shape on the rheological properties of the sintered body. In general, the sintering process was characterized by a decrease in the root-mean-square stress within the porous body matrix to the limiting zero value as it approached the nonporous state and by an increase in the root-mean-square strain rate along the curve with a maximum. Computational modeling of the densification kinetics for the powder composite, involving determination of the activation energy for viscous flow of the composite matrix as a function of temperature and root-mean-square stress, allowed the initial, low-temperature, and medium-temperature stages of spark plasma sintering to be identified. At the initial stage up to 1220 K, the activation energy increased nonlinearly and sharply, which can be caused by active spark flashes with the formation of plasma within the loose random packing of the powder particles, as a similar stage is not observed in conventional pressure assisted sintering. At the next low-temperature temperature stage, the activation energy increased as the root-mean square stress decreased. In the temperature range from 1300 to 1389 K, the activation energy for viscous linear flow of the composite matrix was 223 kJ/mol. In the medium-temperature range from 1414 to 1485 K, the activation energy increased to 255 kJ/mol.

Keywords: *TiB_2–20 wt.% $MoSi_2$ composite, relative density, nonisothermal spark plasma sintering, bulk viscous flow, densification kinetics, activation energy.*

[1]Frantsevich Institute for Problems of Materials Science, National Academy of Sciences of Ukraine, Kyiv, Ukraine.

[2]To whom correspondence should be addressed; e-mail: mskoval@yahoo.com.

Translated from Poroshkova Metallurgiya, Vol. 62, Nos. 1–2 (549), pp. 41–51, 2023. Original article submitted October 6, 2022.

INTRODUCTION

The production of modern hard and refractory materials with enhanced mechanical and functional properties is closely tied to methods used for the forming and pressure sintering of starting powders and their mixtures. Among these methods, spark plasma sintering stands out. Its underlying concept, as described by R.M. German [1], was inspired by the electric furnaces developed by Edward Acheson, notable inventor, and Henri Moissan, Nobel Prize winner. These furnaces employed direct heating of the processed materials by passing electric current through them. At the turn of the 19th and 20th centuries, this method was successfully used to manufacture filaments for electric lighting lamps. The evolution of spark plasma sintering for various metallic, conductive composite, and ceramic materials across different countries throughout the 20th century until 2014 is summarized in the overview paper [2]. This method utilizes rapid heating, along with the application of sufficiently high pressures, to inhibit the grain growth and contribute to the formation of a structure that enhances both the mechanical and functional properties of materials [3–5].

Spark plasma sintering (SPS) is predominantly carried out in graphite dies, as is the case with the hot pressing of powders of refractory materials. These are similar processes, and identical approaches can be applied for their quantitative description and analysis. Therefore, this research used insights from the rheological description of the pressure assisted sintering process within the continuum theory for bulk viscous flow of a porous polycrystalline body [6–11] to analyze the densification kinetics of a powder mixture comprising titanium diboride, TiB_2, with 20 wt.% molybdenum disilicide, $MoSi_2$, during nonisothermal spark plasma sintering at a controlled heating rate.

EXPERIMENTAL PROCEDURE

The TiB_2–20 wt.% $MoSi_2$ mixture, with an average particle size of 200 nm, was produced through two-stage mechanochemical synthesis from the following powders: PT-1 titanium with 20–80 μm particles, PM99.95 molybdenum with 2–5 μm particles, Kr-00 semiconducting silicon, and A99.9 amorphous boron with an average particle size of less than 1 μm [12], employing an AIR-0.01 planetary-ball mill. The powders were ground in steel drums with steel balls under an argon atmosphere at a drum rotation speed of 1370 rpm. The ball-to-powder weight ratio was 10 : 1. The iron content in the mechanochemically synthesized mixtures was no more than 0.92 wt.%.

Spark plasma sintering was carried out using an FCT-HPD25 furnace manufactured by FCT Systems GmbH, capable of reaching a maximum thermodynamic temperature of 2673 K and applying a compression force of 250 kN at a maximum electric current of 8000 A and a maximum voltage of 10 V in a nitrogen atmosphere or in vacuum with a residual pressure of $5 \cdot 10^{-2}$ Pa. Temperature was measured with a pyrometer on the inner surface of the upper graphite punch. Linear shrinkage during the sintering process was captured by tracking the movement of the upper punch provided that the lower punch was fixed. The powders were sintered in a graphite die with an inner diameter of 20 mm at a pressure of 50.93 MPa and at a constant heating rate of 1.67 K/s up to a thermodynamic temperature of 1514 K and at 2.72 K/s above this temperature.

Detailed information on the method for synthesizing and consolidating the TiB_2–$MoSi_2$ composite system can be found in [12].

RESULTS AND DISCUSSION

The current values of the relative density were determined using the current values of the linear shrinkage x_i and final values of the density ς_f and height h_f of the samples with the following equation:

$$\rho = \frac{\varsigma_f h_f}{(h_0 - x_i)\varsigma_{th}}, \quad (1)$$

where $h_0 = h_f + x_f$ is the initial height and ς_{th} is the theoretical density [13].

Experimental data on the time dependence of the relative density of the TiB_2 and $MoSi_2$ powder mixture for nonisothermal SPS are shown in Fig. 1. These data were smoothed using polynomial approximation based on the least squares criterion and verified selectively through the Lagrange polynomials [14].

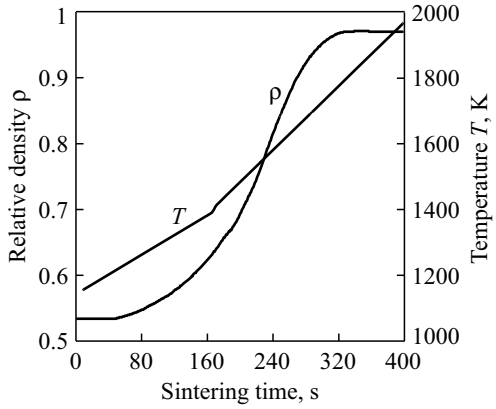

Fig. 1. Time dependences of the relative density ρ and controlled thermodynamic temperature T at a constant heating rate

Within the framework of continuum description and solid mechanics, the composite is macroscopically treated as a homogeneous material, accounting for the properties of its individual components. If the elastic properties of each component are described by Hooke's law, then the elastic behavior of the composite will conform to the same law [15]. Generally, the elastic and rheological properties of multicomponent composites are determined by their most and least stiff components. In our case, the porous composite consists of three components, two of which are similar in properties and constitute the material matrix, while the third component—porosity—lacks material properties. Therefore, we are essentially dealing with a porous matrix composite where the porosity θ or relative density ρ = 1 – θ plays a significant role.

The experimental data (Fig. 1) on the current relative density ρ, densification rate $(\mathrm{d}/\mathrm{d}t)\rho$, and external pressure P acting on the porous body in the die were used to determine the shear root-mean-square stresses $\langle \tau_\mathrm{m} \rangle$ and strain rates $\langle \dot{\varepsilon}_\mathrm{m} \rangle$ in the matrix forming a viscous porous body:

$$\langle \tau_\mathrm{m} \rangle = P\sqrt{\frac{1-2\nu}{\rho\phi(1-\nu)}} = P\sqrt{\frac{2\left(1-\rho^{(1+\rho)/\rho}\right)}{\rho^{m/\rho}\left(2-\rho^{(1+\rho)/\rho}\right)}}; \tag{2}$$

$$\langle \dot{\varepsilon}_\mathrm{m} \rangle = \frac{1}{\rho}\frac{\mathrm{d}\rho}{\mathrm{d}t}\sqrt{\frac{1}{\rho}\left(\psi+\frac{2}{3}\phi\right)} = \frac{1}{\rho}\frac{\mathrm{d}\rho}{\mathrm{d}t}\rho^{(m-2\rho)/(2\rho)}\sqrt{\frac{2-\rho^{(1+\rho)/\rho}}{2\left(1-\rho^{(1+\rho)/\rho}\right)}} \tag{3}$$

where P is the axial pressure; $\nu = \nu_\mathrm{m}\rho^{(1+\rho)/\rho}$; and ν_m is Poisson's ratio of the porous body matrix (ν_m = 1/2 for viscous and plastic bodies). The φ and ψ values were calculated with the equations as follow:

$$\varphi = \rho^{(m-\rho)/\rho};\ \psi = \frac{1}{3}\varphi\frac{1+\nu}{1-2\nu} = \frac{1}{6}\rho^{(m-\rho)/\rho}\frac{2+\rho^{(1+\rho)/\rho}}{1-\rho^{(1+\rho)/\rho}} \tag{4}$$

where m = 2.5 for powder materials formed by an ensemble of regular-shape, nearly spherical particles and m = 3.5 for an ensemble of irregular-shape particles [10, 11].

The current values of the root-mean-square stresses and strain rates of the porous composite matrix were determined with Eqs. (2) and (3), considering the roundness of particles in the powder mixture and using the author's custom code package (Fig. 2). In determining the root-mean-square stress values due to the lack of relevant data, the Laplace pressure was not taken into account. Under the action of the latter during pressureless sintering, the densification of the porous body occurs. During the sintering with assistance of external pressure, its action is additive to the Laplace pressure. Consequently, the obtained data on shear root-mean-square stresses are somewhat underestimated.

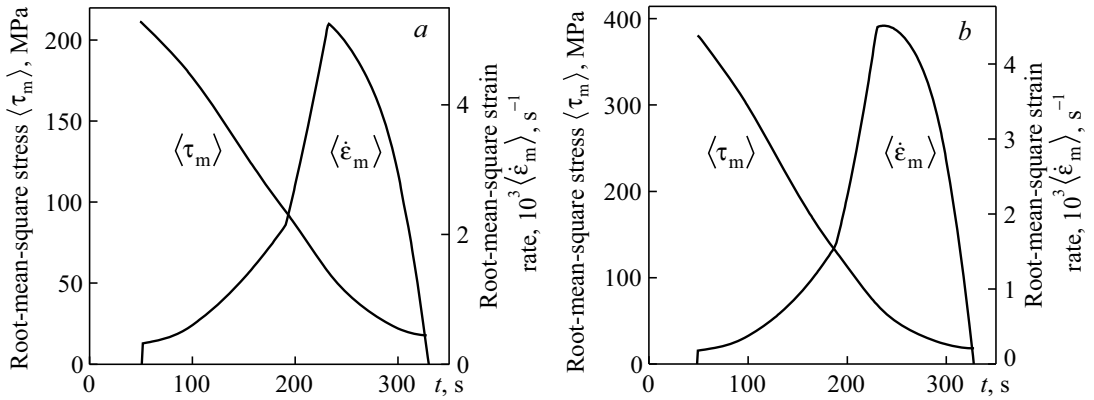

Fig. 2. Time dependences of the root-mean-square stresses and strain rates of the porous composite matrix during spark plasma sintering, considering the roundness of particles: $m = 2.5$ (*a*) and $m = 3.5$ (*b*)

The viscous flow of the porous body matrix is controlled by the mechanisms of nonlinear creep for the crystalline porous body and is described by the equation as follows:

$$\langle \dot{\varepsilon}_m \rangle = \frac{1}{2} A \left(\frac{\langle \tau_m \rangle}{\tau_{m(0)}} \right)^n \tag{5}$$

where n is the nonlinearity exponent for viscous flow. For the dislocation climb mechanism:

$$A = \text{ const } \frac{D_0 \mu_m b}{k_B T} \exp\left(-\frac{U}{k_B T} \right) \tag{6}$$

where D_0 is the preexponential factor for the bulk self-diffusion coefficient; U is the activation energy; μ_m is the shear elastic modulus; b is the Burgers vector; T is the thermodynamic temperature; k_B is the Boltzmann constant; and $\tau_{m(0)}$ is the shear yield stress of the matrix material [16].

The substitution of Eqs. (2) and (3) into (5) gives the equation for the pressure sintering kinetics for a porous crystalline body in a die:

$$\rho^{\frac{2.5(n+1)-4\rho}{2\rho}} \left(\frac{2-\rho^{(1+\rho)/\rho}}{2\left(1-\rho^{(1+\rho)/\rho}\right)} \right)^{\frac{n+1}{2}} \frac{d\rho}{dt} = \frac{1}{2} A \left(\frac{P}{\tau_{m(0)}} \right)^n = \frac{d}{dt} X_{d(2)}(n, \rho) = \dot{X}_{d(2)}(n,\rho), \tag{7a}$$

$$\rho^{\frac{3.5(n+1)-4\rho}{2\rho}} \left(\frac{2-\rho^{(1+\rho)/\rho}}{2\left(1-\rho^{(1+\rho)/\rho}\right)} \right)^{\frac{n+1}{2}} \frac{d\rho}{dt} = \frac{1}{2} A \left(\frac{P}{\tau_{m(0)}} \right)^n = \frac{d}{dt} X_{d(3)}(n, \rho) = \dot{X}_{d(3)}(n,\rho) \tag{7b}$$

where $X_{d(2)}(n,\rho)$ and $X_{d(3)}(n,\rho)$ are the integral functions of the relative density obtained by integrating the left-hand terms of Eqs. (7a) and (7b):

$$X_{d(2)}(n,\rho) = \int_{\rho_0}^{\rho} \rho^{\frac{2.5(n+1)-4\rho}{2\rho}} \left(\frac{2-\rho^{(1+\rho)/\rho}}{2\left(1-\rho^{(1+\rho)/\rho}\right)} \right)^{\frac{n+1}{2}} d\rho\,; \tag{8a}$$

$$X_{d(3)}(n,\rho) = \int_{\rho_0}^{\rho} \rho^{\frac{3.5(n+1)-4\rho}{2\rho}} \left(\frac{2-\rho^{(1+\rho)/\rho}}{2\left(1-\rho^{(1+\rho)/\rho}\right)} \right)^{\frac{n+1}{2}} d\rho. \tag{8b}$$

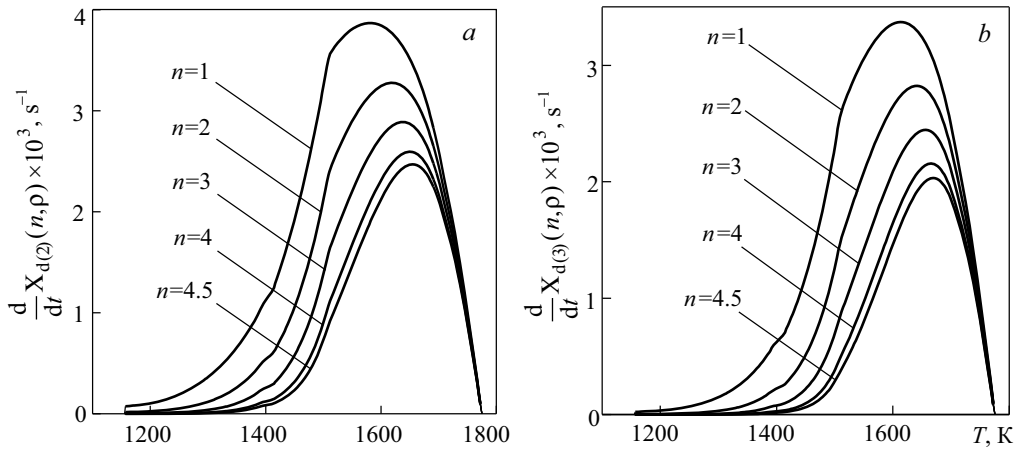

Fig. 3. Computational modeling of the temperature dependence of densification kinetics $\dot{X}_{d(2)}(n,\rho)$ (*a*) and $\dot{X}_{d(3)}(n,\rho)$ (*b*) for the composite during SPS

Computational modeling of the densification kinetics of the composite during SPS, based on the experimental data (Fig. 1), using Eqs. (7a) and (7b), is presented in Fig. 3 where each discrete point of the calculated kinetics corresponds to the initial points in Fig. 1, with the current temperature values recorded at intervals of 1 s.

The ratio of the densification kinetics of a porous body, described by Eqs. (7a) and (7b) taking into account Eq. (6), at two selected temperatures is expressed as follows:

$$\frac{T_2\dot{X}^{(2)}_{d(2)}(n,\rho)}{T_1\dot{X}^{(1)}_{d(2)}(n,\rho)} = \exp\left\{\frac{U}{k_B}\left(\frac{1}{T_1}-\frac{1}{T_2}\right)\right\}. \tag{9}$$

Taking the logarithm and performing minor transformations of this equation lead to the well-known equation for estimating the activation energy:

$$U = k_B\frac{T_1T_2}{T_2-T_1}\left\{\ln\frac{T_2\dot{X}^{(2)}_{d(2)}(n,\rho)}{T_1\dot{X}^{(1)}_{d(2)}(n,\rho)}\right\}. \tag{10}$$

According to these equations, the activation energy at constant initial temperature T_0 is determined from the dependences of $\ln\left\{T\dot{X}_{d(2)}(n,\rho)\right\}$ and $\ln\left\{T\dot{X}_{d(3)}(n,\rho)\right\}$ logarithms on reciprocal thermodynamic temperature T^{-1}.

The rate of changes in the relative density function on the ascending sections of the curves in Fig. 3 was used to determine the $\ln\left\{T\dot{X}_{d(2)}(n,\rho)\right\}$ and $\ln\left\{T\dot{X}_{d(3)}(n,\rho)\right\}$ logarithms as a function of reciprocal thermodynamic temperature T^{-1} (Fig. 4). These curves feature two temperature ranges: 1414 K ≤ T ≤ 1485 K and 1311 K ≤ T ≤ 1389 K, over which these dependences are linear with a high correction coefficient (r = 0.9998), and the activation energy corresponds to the slope of the straight lines to the reciprocal temperature axis. The data obtained are presented in Tables 1 and 2.

At the initial stages of nonisothermal spark plasma sintering, nonlinear dependences of $\ln\left\{T\dot{X}_{d(2)}(n,\rho)\right\}$ and $\ln\left\{T\dot{X}_{d(3)}(n,\rho)\right\}$ logarithms on reciprocal temperature are observed, as shown in Fig. 4. This indicates that the activation energy is dependent on the root-mean-square stress in the porous composite matrix. The current values of the activation energy were determined from the slope of the $\ln\left\{T\dot{X}_{d(2)}(n,\rho)\right\}$, and $\ln\left\{T\dot{X}_{d(3)}(n,\rho)\right\}$ logarithmic curves to the reciprocal temperature axis. The activation energies determined as a function of the root-mean square stresses in the porous composite matrix are provided in Fig. 5.

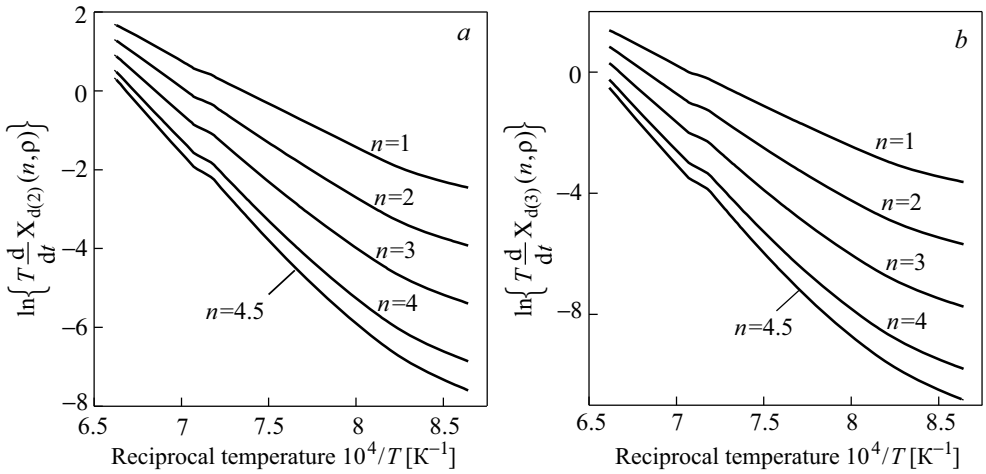

Fig. 4. Logarithms $\ln\left\{T\dot{\mathrm{X}}_{\mathrm{d}(2)}(n,\rho)\right\}$ (*a*) and $\ln\left\{T\dot{\mathrm{X}}_{\mathrm{d}(3)}(n,\rho)\right\}$ (*b*) vs reciprocal thermodynamic temperature T^{-1}

Figure 5 shows that the lowest values of the activation energy increase non-linearly in the temperature range from 1155 to 1225 K. This type of relationship between the activation energy and stresses has not been observed previously during the pressure sintering of powders. Therefore, it can be surmised that this behavior is unique to spark plasma sintering and probably results from spark flashes in the small gaps between powder particles in their random loose packing. At a temperature of 1237 K, the stage of a slow increase in activation energy with a decrease in stresses within the material occurs and is characteristic of low-temperature pressure sintering [11].

TABLE 1. Activation Energy for Viscous Flow of the Porous Composite Matrix in the Temperature Range 1414 K ≤ T ≤ 1485 K

Flow nonlinearity exponent n	Activation energy (kJ/mol) for the logarithm of the integral relative density function	
	$\ln\left\{T\dot{\mathrm{X}}_{\mathrm{d}(2)}(n,\rho)\right\}$	$\ln\left\{T\dot{\mathrm{X}}_{\mathrm{d}(3)}(n,\rho)\right\}$
1	209.4	255.4
2	267.1	336.1
3	324.4	416.7
4	381.7	497.3
4.5	410.4	537.6

TABLE 2. Activation Energy for Viscous Flow of the Porous Composite Matrix at Temperatures Below 1389 K

Flow nonlinearity exponent n	Temperature range, K	Activation energy (kJ/mol) for the logarithm of the integral relative density function	
		$\ln\left\{T\dot{\mathrm{X}}_{\mathrm{d}(2)}(n,\rho)\right\}$	$\ln\left\{T\dot{\mathrm{X}}_{\mathrm{d}(3)}(n,\rho)\right\}$
1	1300 ≤ T ≤ 1389	182.7	223.0
2	1310 ≤ T ≤ 1389	245.6	326.2
3	1311 ≤ T ≤ 1389	307.1	407.3
4	1311 ≤ T ≤ 1389	369.2	493.5
4.5	1322 ≤ T ≤ 1389	404.5	543.9

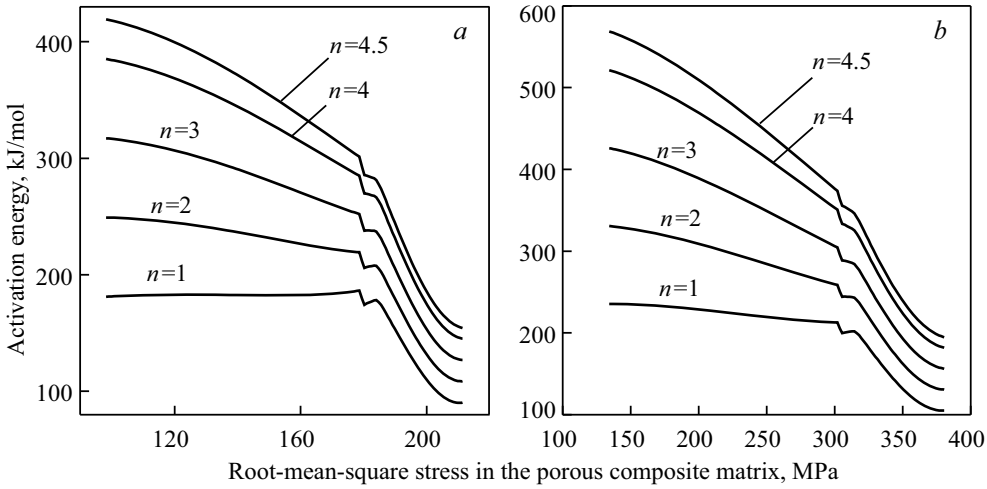

Fig. 5. Activation energy for viscous flow of the porous composite matrix determined from $\ln\left\{T\dot{\mathrm{X}}_{\mathrm{d}(2)}\left(n,\rho\right)\right\}$ (*a*) and $\ln\left\{T\dot{\mathrm{X}}_{\mathrm{d}(3)}\left(n,\rho\right)\right\}$ (*b*) logarithms vs root-mean square stresses at the initial SPS stages

The activation energy U as a function of the root-mean-square stress in the porous body matrix $\left\langle\tau_{\mathrm{m}}\right\rangle$ is expressed by the following equation:

$$U = U_0 - v_{\mathrm{a}}\left\langle\tau_{\mathrm{m}}\right\rangle \tag{11}$$

where v_{a} is the activation volume [16, 17]. The calculated U and v_{a} values are provided in Table 3.

Since the root-mean-square stress values are somewhat underestimated, as noted above, the activation volume values are somewhat overestimated. However, this does not compromise the validity of the observed trend.

The lowest curve in Fig. 5*a* does not display a decrease in the activation energy with an increase in the root-mean-square stress in the composite matrix, contrastingly to all other curves. This indicates that the densification kinetics peculiar to powders with particles of mostly regular, near-spherical shape is not applicable to the composite under study. Hence, the densification kinetics is described by Eq. (7b) with the boundary linear viscous exponent n = 1, because $n > 1$ corresponds to rather high activation energies, which are characteristic of

TABLE 3. Initial Values of the Activation Energy and Activation Volume at the Low-Temperature Spark Plasma Sintering Stage

Sintering kinetics	Activation energy U_0, kJ/mol	Activation volume v_{a}, m^3
$\dot{\mathrm{X}}_{\mathrm{d}(2)}\left(n=2,\ \rho\right)$	301.7639	$4.675938 \cdot 10^{-4}$
$\dot{\mathrm{X}}_{\mathrm{d}(2)}\left(n=3,\ \rho\right)$	431.1386	$1.003898 \cdot 10^{-3}$
$\dot{\mathrm{X}}_{\mathrm{d}(2)}\left(n=4,\ \rho\right)$	463.8479	$1.560238 \cdot 10^{-3}$
$\dot{\mathrm{X}}_{\mathrm{d}(2)}\left(n=4.5,\ \rho\right)$	633.0847	$1.855567 \cdot 10^{-3}$
$\dot{\mathrm{X}}_{\mathrm{d}(3)}\left(n=1,\ \rho\right)$	261.610	$1.667080 \cdot 10^{-4}$
$\dot{\mathrm{X}}_{\mathrm{d}(3)}\left(n=2,\ \rho\right)$	409.5893	$5.013992 \cdot 10^{-4}$
$\dot{\mathrm{X}}_{\mathrm{d}(3)}\left(n=3,\ \rho\right)$	561.5974	$8.509330 \cdot 10^{-4}$
$\dot{\mathrm{X}}_{\mathrm{d}(3)}\left(n=4,\ \rho\right)$	719.0676	$1.219913 \cdot 10^{-3}$
$\dot{\mathrm{X}}_{\mathrm{d}(3)}\left(n=4.5,\ \rho\right)$	797.7234	$1.404037 \cdot 10^{-3}$

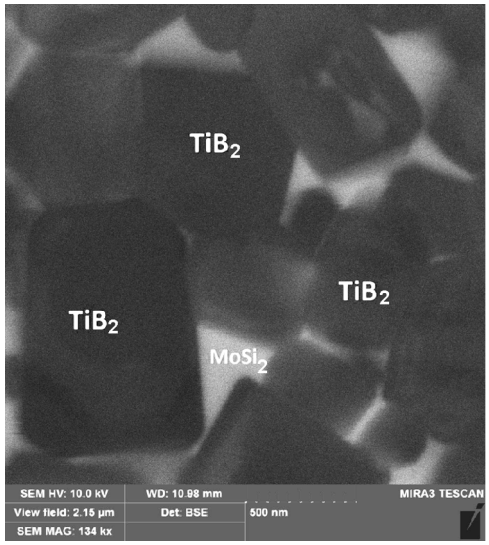

Fig. 6. Structure of the TiB_2–20 wt.% $MoSi_2$ composite consolidated by spark plasma sintering

high-temperature strain mechanisms associated with dislocation climbs. Low-temperature strains may be corresponding to thermally activated sliding the dislocations. The flow linearity is indirectly confirmed by studies on isothermal spark plasma sintering of nanosized tantalum carbide powder [18], carried out employing the described method.

The structure of the sintered samples analyzed using scanning electron microscopy with a Mira 3 microscope (Tescan) showed small titanium diboride grains with sizes up to 500 nm (Fig. 6).

CONCLUSIONS

Computational analysis of the densification kinetics for a powder mixture containing 80 wt.% titanium diboride and 20 wt.% molybdenum disilicide during nonisothermal spark plasma sintering assisted with an external pressure of 50.93 MPa in vacuum at a controlled constant heating rate of 1.67 and 2.72 K per second was carried out within the continuum theory for bulk viscous flow of porous bodies.

The initial thermodynamic temperature, at which the sintering process begins, was experimentally established. This temperature, which is 1155 K, should be considered the critical brittle–ductile transition temperature for less refractory molybdenum disilicide.

The determination of time-dependent rheological characteristics of the composite during sintering shows that the root-mean-square stress in the porous composite matrix naturally decreases as the relative density increases, while the root-mean-square strain rate of the matrix does not decrease but rather follows a curve with a maximum, contrary to what occurs in isothermal sintering. The effect exerted by the shape of the powder particles on the rheological properties of the composite, which determine its densification kinetics, is taken into account.

The dependence of the activation energy for viscous flow of the porous composite matrix on temperature and root-mean-square stress revealed the presence of initial, low-temperature, and medium-temperature stages in spark plasma sintering.

In the initial stage (up to 1220 K), the activation energy increases nonlinearly and sharply, which may be indicative of active sparks with the formation of plasma in the loosely packed random ensemble of powder particles. This stage is not observed during conventional pressure sintering. In the subsequent, low-temperature stage, the activation energy increases as the root-mean-square stress decreases. In the temperature range from 1220 to 1389 K, the activation energy for linear viscous flow of the composite matrix is 223 kJ/mol. In the medium-temperature range, from 1414 to 1485 K, the activation energy slightly increases to 255 kJ/mol.

REFERENCES

1. R.M. German, *Sintering Science: An Historical Perspective*, copyright © 2016 Randall M. German, https://www.academia.edu.
2. O. Guillon, J. Gonzalez-Julian, B. Dargatz, T. Kessel, G. Schierning, J. Rathel, and M. Herrmann, "Field-assisted sintering technology/spark plasma sintering: Mechanisms, materials, and technology developments," *Adv. Eng. Mater.*, **16**, No. 7, 830–849 (2014), doi: 10.1002/adem.201300409.
3. P. Tanaji and P.H. Sandip, "Initial stage densification during spark plasma sintering of Fe-based amorphous alloy powder: Analysis of viscous flow," *J. Appl. Phys*., **120**, 134901 (2016), https://doi.org/10.1063/1.4964330.
4. M.S. Boldin, A.A. Popov, E.A. Lantsev, A.V. Nokhrin, and V.N. Chuvil'deev, "Investigation of the kinetics of spark plasma sintering of alumina ceramics. Part 1. The initial stage of sintering," *IOP Conf. Ser. Mater. Sci. Eng.*, **558**, 012005 (2019).
5. M. Stuer, P. Bowen, and Z. Zhao, "Spark plasma sintering of ceramics: From modeling to practice," *Ceramics*, **3**, 476–493 (2020), doi:10.3390/ceramics 3040039.
6. V.V. Skorokhod, *Rheological Fundamentals of Sintering Theory* [in Russian], Naukova Dumka, Kyiv (1972), p. 151.
7. M.S. Kovalchenko, "Pressure sintering of powder materials," *Powder Metall. Met. Ceram.*, **50**, No. 1–2, 18–33 (2011).
8. M.S. Kovalchenko, "Rheological models of pressure sintering of powders," *Powder Metall. Met. Ceram.*, **52**, No. 1–2, 7–19 (2013).
9. M.S. Kovalchenko, "Rheology and kinetics of pressure sintering," *Mater. Sci. Forum*, **835**, 76–105 (2016).
10. M.S. Kovalchenko, Yu.G. Tkachenko, D.Z. Yurchenko, and V.F. Britun, "Nonisothermal pressure sintering kinetics of the B_4C–SiC powder mixture, structure and fracture behavior of sintered composite," *Powder Metall. Met. Ceram.*, **53**, No. 3–4, 180–190 (2014).
11. M.S. Kovalchenko, V.B. Vinokurov, R.V. Litvin, and L.I. Klimenko, "The densification kinetics of porous zirconium diboride in vacuum pressure sintering," *Powder Metall. Met. Ceram.*, **60**, No. 5–6, 278–290 (2021).
12. O. Zgalat-Lozynskyy, I. Kud, L. Ieremenko, D. Zyatkevych, L. Krushynska, R. Lytvyn, O. Myslyvchenko, O. Tolochyn, and D. Verbylo, "Preparation of TiB_2–20 wt.% $MoSi_2$ composite material by mechanochemical synthesis and spark plasma sintering," *Metall. Mater. Trans*. *A*, **52**, 2451–2462 (2021), DOI.ORG/10.1007/S11661-021-06235-3.
13. M.S. Kovalchenko, "Pressure sintering kinetics of tungsten and titanium carbides," *Int. J. Refract. Met. Hard Mater*., **39**, 32–37 (2013).
14. A. Angot, *Mathematics for Electrical and Telecommunications Engineers* [in French], Éditions de la Revue d'Optique, Paris (1949), p. 660.
15. T.D. Shermergor, *Elasticity Theory for Microheterogeneous Media* [in Russian], Nauka, Moscow (1977), p. 400.
16. D.S. Wilkinson and M.F. Ashby, "Pressure sintering by power law creep," *Acta Met.*, **23**, 1277–1285 (1975).
17. J. Friedel, *Dislocations*, Pergamon Press, Oxford–London–Edinburgh–New York–Paris–Frankfurt (1964), p. 512.
18. G.P. Cherepanov, "Chapter 4. Physics of sintering," in: *Solid Mechanics and Its Applications. Vol. 51: Methods of Fracture Mechanics: Solid Matter Physics*, Kluwer Acad. Publ., Dordrecht (1997), p. 333.
19. A. Nisar, S. Ariharan, and K. Balani, "Densification kinetics and mechanical properties of tantalum carbide," *Int. J. Refract. Met. Hard Mater*., **73**, 221–230 (2018).